

Structure and dynamics of uranium dioxide up to melting

L. B. Skinner^{1,2,3}, C. J. Benmore¹, J. K. R. Weber³, M. A. Williamson⁴, A. Tamalonis³, A. Hebden⁴, T. Wiencek⁵, O.L.G. Alderman³, M. Guthrie⁶, L. Leibowitz⁴, J. B. Parise²

¹X-ray Science Division, Argonne National Laboratory, Argonne, IL 60439, USA.

²Mineral Physics Institute, Stony Brook University, Stony Brook NY 11794-2100, USA.

³Materials Development, Inc., 3090 Daniels Court, Arlington Heights, IL 60004, USA.

⁴Chemical Science & Engineering, Argonne National Laboratory, Argonne, IL 60439, USA.

⁵Nuclear Engineering, Argonne National Laboratory, Argonne, IL 60439, USA.

⁶Geophysical Laboratory, Carnegie Institution of Washington, Washington DC 20015, USA.

Contributions:

LBS original idea, wrote proposal, wrote paper, data analysis, MD simulations.

CJB safety exp. planning, manuscript prep., data analysis.

JKRW original idea, exp. planning, equipment prep.

MW safety, exp. planning, sample prep.

AT equipment design & prep.

AH TW chamber design, sample prep.

OLGA experiment, contributions to manuscript.

MG, LL, JD, JBP, contributions to manuscript.

*****Introductory paragraph***

Uranium dioxide (UO₂) is the major fuel component for most nuclear power reactors in use today, even mixed oxide fuel is typically 90% UO₂. A key concern during severe accidents is the melting and subsequent leakage of radioactive UO₂ as it corrodes through its Zr-cladding and steel containment. Yet, the very high temperatures (>3140 K) and the chemical reactivity of the melt have prevented structural studies of molten UO₂¹⁻⁵. In this work we use laser heating and sample levitation to obtain x-ray pair distribution function measurements of hot solid and liquid UO₂. These measurements show a substantial increase in oxygen disorder around the lambda transition (2670K), followed by a drop in the average U-O coordination number from 8 to 6.7(5) upon melting. These measurements are used to refine molecular dynamics (MD) models which predict greatly increased U-U mobility in the melt compared to the hot solid.

*****Main text***

Unlike its structure, many of the physical properties of liquid UO₂ have been measured. Although large uncertainties remain for several properties relevant to reactor safety, high temperature experiments have yielded values for heat capacity, surface tension, density, and others (see review of¹). Density in particular is key to the liquid structure and the value 8.86gcm⁻³ corresponds to a 9.6% density decrease on melting¹. To understand these structure-property relations in UO₂ and predict its interaction with other materials at high temperatures, we have investigated the structure changes associated with this density drop through x-ray pair distribution function measurements and MD simulations.

Although several literature MD models exist for UO₂, they differ significantly in their melt structure predictions. The liquid U-O bond length r_{UO} , for example, varies from 1.9 Å to 2.2 Å between literature models⁵⁻⁹. The present x-ray measurements, by contrast, find $r_{\text{UO}} = 2.22(1)$ Å (at 3270 K). Prior to melting, hot solid UO₂ also undergoes a superionic lambda transition at 2670 K which is characterized by rapidly increasing oxygen disorder⁵. Approaching this lambda transition there are steep rises in heat capacity and thermal conductivity¹. Though some MD models predict local structure changes and reduced U-O coordination through the lambda transition, other models retain their local structure through into the melt⁶. The present x-ray measurements show that the U-O coordination stays close to 8, while these UO₈ polyhedra become significantly distorted through the lambda transition. Upon melting, however, the average U-O coordination drops to around 6.7(5), while the U-U correlations become much more disordered.

Synchrotron x-ray diffraction measurements were performed on depleted UO₂ which was laser heated while suspended in an aerodynamic levitator. This method involved the floating of a 3mm ball-shaped sample on an Ar gas stream inside a high purity Ar filled chamber¹⁰. The absence of any solid contact with the very hot sample allows its chemical purity to be maintained. High energy x-rays (111.158 keV) were used to minimize absorption and multiple scattering in the sample. Scattered x-ray intensity vs. angle was measured using an area detector and analyzed using standard methods (see methods).

After corrections, these x-ray measurements yield the x-ray structure factor, $S_x(Q)$, where Q is momentum transfer given by $Q = 4\pi\sin(\theta) / \lambda$, 2θ is the scattering angle, λ is the incident x-ray wavelength (see¹¹ for further detail). The measured $S_x(Q)$ is then Fourier transformed to give the pair distribution functions ($g(r)$, $D(r)$, or $T(r)$) which describe the probability of finding atom pairs with a given separation r (see methods). Peak positions in these pair distribution functions correspond to inter-atomic separation distances, peak areas provide coordination numbers, and peak widths provide information on the local disorder. As an approximate guide, x-ray diffraction patterns on UO₂ consist of partial pair contribution weightings of 73% U-U, 25% U-O, and 2% O-O (at $Q = 0$).

Figure 1A shows the measured diffraction patterns at several temperatures and the experimental setup (inset). Above 1300K the high- Q region ($Q > 12 \text{ \AA}^{-1}$) contained no significant structure. The consistent Bragg peak positions and relative intensities indicate that the long-range U-U order of the CaF_2 -like cubic structure is maintained through the entire solid UO_2 temperature range, including above the lambda transition. While the reduced intensity of high- Q Bragg peaks at high temperatures indicates increasing disorder. The corresponding $D_X(r)$ patterns (Fig. 1b) also confirm the consistent U-U periodicity, expansion, and increasing disorder with increasing temperature. The $D_X(r)$ of the Yakub MD model⁵ is shown above and below the lambda transition (dotted lines, Fig 1b) and displays structure which closely matches the hot-solid measurements. Of the literature models investigated^{6-9,12}, this Yakub MD model is found to be the closest match to the present $D_X(r)$ measurements.

Despite normal volume expansion, the measured U-O bond length, r_{UO} (from $T_X(r)$ peak maxima), contracts on heating up to the melting point, whereas r_{UU} expands (Fig. 2b). This r_{UO} contraction and r_{UU} expansion also matches the Yakub MD model. What then is happening to the U-O coordination as r_{UO} contracts? To answer this, the running coordination numbers $n_{ij}(r)$, which give the average number of atoms of type j around type i within a distance r , are plotted (where i, j represent atomic species, Fig. 2 a,c). Note the $n_{ij}(r)$ is obtained from the integral of the $rT_{ij}(r)$ pair distribution function^{11,13}. Measured $n_{\text{UO}}(r)$ curves are also obtained by reweighting and integrating the x-ray patterns (Fig 2A circles, see¹⁴ for detail). Above 3 \AA , however, U-U correlations start to contribute to the x-ray pattern, limiting the range of applicability of the measured $n_{\text{UO}}(r)$. The Yakub MD simulations, which closely agree with the x-ray measurements, allow full isolation of U-U and U-O correlations. These isolated $n_{\text{UO}}(r)$ and $n_{\text{UU}}(r)$ curves from the MD model also demonstrate the ambiguity in assigning a single number to average coordination. While at low temperatures the n_{UO} and n_{UU} are unambiguously 8 and 12 respectively, as the temperature increases the $n_{ij}(r)$ curves no longer plateau, introducing significant cut-off dependence. Taking the coordination up to the minimum in $rT_{ij}(r)$ (the inflection point in $n_{ij}(r)$), the coordination numbers remain close to $n_{\text{UO}} = 8$ and $n_{\text{UU}} = 12$ up to the melting point. At high temperatures, however, there are fewer short U-O neighbors ($< 2.8 \text{ \AA}$), and more long U-O neighbors (2.8 to 3.5 \AA), in the hot solid compared to lower temperatures.

In the melt, the first U-O peak in $T(r)$ is only slightly broader and slightly shorter than in the hot solid, but the n_{UO} coordination is significantly lower (Fig. 2a). The U-U peak undergoes much larger broadening and shortening on melting, with a smaller drop in coordination (Fig. 2. b,c). This indicates a significant change from the UO_8 cubic polyhedra of the solid, and a very large broadening of the local U-U arrangements, which describe how the U-O polyhedra are connected in the melt. Also unlike crystalline UO_2 , the r_{UO} in the liquid state expands normally in the MD models investigated (Fig. 2B). Although this expansion of r_{UO} in the liquid cannot be confirmed by the single temperature point measured, first peak contraction behavior is not generally expected in oxide melts. Measurements on CaAl_2O_4 and SiO_2 liquids, for example, show expansion of r_{AlO} , r_{SiO} despite slightly reducing n_{AlO} and n_{SiO} coordination on heating^{14,15}. This behaviour is in contrast to several liquid metals which have been shown to display contraction in the first peak in $g(r)$ on heating¹⁶. The Yakub and refined MD models currently investigated display r_{UO} expansion in the melt, while also reproducing the measured contraction of r_{UO} of the hot crystalline solid.

Further inspection of the UO_2 liquid structure is given in Figure 3. The x-ray measurements yield $r_{\text{UO}} = 2.22(1) \text{ \AA}$, $r_{\text{UU}} = 3.88(10) \text{ \AA}$, and $n_{\text{UO}} = 6.7(0.5)$, the latter two of which are matched within error by the Yakub MD model. Discrepancies remain, however, in the first peaks of both $S_X(Q)$ and $g_X(r)$ (r_{UO} of the Yakub model is $2.24(1)$). To address these discrepancies a simple pair potential model using the Morse functional form was refined against the measured liquid structure. This refinement involved adjusting the U-O and O-O potentials until the model was in closer agreement with the measured liquid $T(r)$ and density. After refinement, the UO_2 MD model essentially reproduces the $S_X(Q)$ measurement within error apart from the first peak in $S_X(Q)$ which is slightly sharper in the MD model than the measurement. The effect of the sharp $S_X(Q)$ peak on the $g_X(r)$ is visible in the $r > 5 \text{ \AA}$ oscillations which have slightly different damping and amplitude in the MD models compared to the x-ray measurement.

The CaF₂-like cubic crystal structure of UO₂ consists of UO₈ cubic polyhedra that share every edge with one of 12 neighboring polyhedra, such that looking out from each U through the faces of the UO₈ cube there is a gap to the next U which is a distance $2r_{\text{OO}}$ away (see figure 3c). After melting, the refined MD model finds the lower coordinated liquid to be approximately 40(5)% UO₆ and 40(5)% UO₇, with the remaining 20% being mainly UO₅ and UO₈. Accompanying this lower n_{UO} is the reduced sharing of oxygen with $\sim 2/3$ of the O shared between just 3, rather than 4 UO_x polyhedra as in the crystal. Similarly, the connectivity of the UO_x polyhedra reduces from 100% edge shared in the crystal to 60% corner-shared, 33% edge shared and 7% face shared in the melt. The predominance of two coordination species in the melt also raises the question: Do these UO₆, UO₇ have a preference to cluster together or avoid each other? This question was investigated by defining two U sub-species U6 (U with $n_{\text{UO}} \leq 6$) and U7 ($n_{\text{UO}} \geq 7$). The distribution of U6 and U7 subspecies is then investigated through the Bhatia-Thornton concentration-concentration pair distribution function ($g_{\text{cc}}(r)$)¹⁷. Positive values of $g_{\text{cc}}(r)$ indicate a preference for neighbors of like subspecies, whereas negative values indicate a preference for unlike subspecies. Here, the small peak in $g_{\text{cc}}(r)$ (Figure 3b) indicates a slight preference for U6-U6 and U7-U7 connections over U6-U7 and U7-U6 connections, implying only very slight clustering of these polyhedral types.

One explanation for the minimal clustering is rapid rearrangement of the local polyhedra in the melt. To investigate the dynamic rearrangement of structural units, the rate at which atoms move out of the first coordination sphere (bond breaking) was investigated in the refined MD model. Defined as the separation not exceeding a given cut-off value (r_{cut}), the probability of bond survival, was found to have roughly stretched exponential decay ($\exp(-at^b)$, $b < 1$). For simplicity, just the time for 50% of initially bound pairs to experience a breaking event (τ_{50}) is investigated. Comparing these bond “half-lives” in the supercooled melt at 3000K to the crystalline solid at the same temperature shows similar U-O τ_{50} values of 0.46 ps (liquid) vs. 0.53 ps (crystal) ($r_{\text{cut}} = 3.1 \text{ \AA}$, Fig. 3a inset). This means that O are being rapidly exchanged between U atoms in both the liquid and hot solid i.e. the U-O polyhedra do not move around as intact UO_{6,7,8} units for any significant time. The U-U correlations, however, were found to swap neighbors more slowly, taking 1.6 ps, in the liquid and 8.3 ps in the crystalline solid at 3000K ($r_{\text{cut}} = 5.1 \text{ \AA}$, Fig. 3a inset). This greatly increased U-U mobility in the liquid is coincident with the collapse of the ordered U-U lattice, whereas the similarity of the U-O τ_{50} values is consistent with the disordered “liquid like” O positions in the post lambda transition hot solid. The U-O and U-U τ_{50} times in the liquid at 3270K were 0.42 ps and 1.3 ps, which are slightly faster than the supercooled liquid at 3000K. The individual U and O diffusion rates of the refined MD model also tell a similar story: Below the lambda transition (2670K) there is negligible U or O diffusion on the ~ 100 ps timescales investigated. Past the lambda transition at 3000K, the crystalline O diffusion has increased to $5.1 \text{ nm}^2 \text{ s}^{-1}$, while the U diffusion remains below $10^{-4} \text{ nm}^2 \text{ s}^{-1}$. In the liquid state, however, the U and O diffusion rates are a similar magnitude (3.7 vs. $9.3 \text{ nm}^2 \text{ s}^{-1}$ at 3270K). Using pressure, an 8-coordinated UO₂ melt can be simulated at a number density of 0.074 \AA^{-3} . The 8-coordinated melt has 3 times slower U and O diffusion rates (1.2 and $3.8 \text{ nm}^2 \text{ s}^{-1}$) than the low-coordinated melt.

Slices of the hot solid and liquid UO₂ MD simulations (Fig 3c) illustrate the large oxygen disorder above the lambda transition and the different UO_{6,7} coordination species which predominate in the melt. The structure and optimized inter-atomic potentials for UO₂ provided in this work allow for accurate atomistic multi-scale modelling to be performed with relatively low computational effort. The present x-ray data, are provided in the supplemental information, and may be used as an end-member structure benchmark for models which extend to multicomponent systems such as corium melts and high level waste glasses.

Methods

X-ray experiments were performed at sector 11-ID-C of the Advanced Photon Source (Argonne, IL, USA). Scattered x-rays were detected using a Perkin Elmer XRD1621 amorphous silicon area detector. The sample-detector distance was calibrated using a NIST standard CeO₂ powder sample. X-ray transmission through the UO₂ sample ~50% was achieved by using a thin incident beam (0.2mm vertical width) and scanning the sample stage such that diffraction was measured from the top 0.2mm of the molten drop. The sample was levitated on a 99.999% pure Ar gas stream, and heated from above using a 400W CO₂ laser (Synrad Firestar i401). Temperature was measured at the top of the sample using a Chino IR-CAS pyrometer (0.7-0.9μm waveband). The liquid UO₂ emissivity value of 0.84(3) was used in the temperature correction¹⁸ and the error in temperature is estimated to be ~2-3% due to temperature gradients in the upper part of the sample measured and chamber window transparency corrections. A brass sheet was placed in front of the area detector to absorb any uranium fluorescence (L-edge ~20keV), while passing >80% of the elastically scattered x-rays (standard corrections were used for attenuation¹⁹). The 2D scattering patterns were integrated using Fit2D²⁰. The Q -resolution of the setup was found to be approximately constant at ~0.05Å⁻¹ from the FWHM of calibration peaks for $Q < 10$ Å⁻¹. For reference the first peak in the liquid UO₂ $S_X(Q)$ had a FWHM ~0.5Å⁻¹. A similar setup has recently been used to obtain partial structure factor information from rare earth oxide liquids²¹.

For full comparison to the x-ray measurement the MD simulated U-U, U-O and O-O partial structure factors were weighted using the Q -dependent x-ray form factors, including dispersion terms for U, and by combining formal charge and neutral form factors²²⁻²⁴ in a 50:50 ratio to approximate partial covalence. The x-ray weighted pattern was then Fourier transformed using the same transform parameters as the measured x-ray data. Specifically $g_X(r)$ is related to the measured structure factor $S_X(Q)$ by

$$g_X(r) - 1 = \frac{1}{2\pi^2 \rho r} \int_0^{Q_{\max}} Q(S_X(Q) - 1)M(Q, \Delta) \sin(Qr) dQ \quad (1)$$

Where ρ is the number density in atoms per Å³ (0.0593Å⁻³ for liquid UO₂), and the modification function $M(Q, \Delta)$ is used to discriminate against unphysical high frequency noise in the liquid $g(r)$ patterns (Figure 3), while avoiding broadening of real features in $g(r)$ (Δ is an r -space averaging width which may vary with r ^{13,14}). For the hot solid patterns in Figures 1 and 2 $M(Q, \Delta) = 1$ is used to avoid broadening. The $D(r)$ and $T(r)$ functions (figures 1 and 2) emphasize higher- r correlations and are related to $g(r)$ by $D(r) = 4\pi\rho r(g(r) - 1)$ and $T(r) = 4\pi\rho r g(r)$ (for further detail see^{11,13,14}). Bond lengths reported are determined from the relevant peak maximum positions in $T_X(r)$ or $T_{ij}(r)$ functions.

MD simulations were performed using the DL_POLY classic package²⁵. Liquid simulations were initiated from random configurations where all atoms had been moved to have a minimum separation of 1.5Å. Simulations were then run under NPT conditions at 6000K for 50ps, and 4000K for 50ps before running at experimental temperatures each for 100ps, configurations were collected and analyzed from the last 50ps of each 100 ps run. Crystalline configurations were initiated from the crystal structure of²⁶ using a box size of 8x8x8 unit cells. This crystal was run at 300K for 200ps before temperatures were increased to the experimental values. Again each temperature step was run under NPT conditions for 100ps with only the last 50ps used in the analysis. The Morse potentials used for the refined model are given by

$$U_{ij}(r) = \frac{e^2}{4\pi\epsilon_0} \frac{z_i z_j}{r} + D_{ij} \exp(-2W_{ij}(r - R_{ij})) - 2D_{ij} \exp(-W_{ij}(r - R_{ij})) \quad (2)$$

where $z_U = 2.2$, $z_O = -1.1$, were chosen to be close to the Yakub model, and the refined constants D_{ij} , W_{ij} , and R_{ij} were 0.21 eV, 1.5 Å⁻¹, and 2.880 Å for U-O and 0.02 eV, 1.48 Å⁻¹, and 3.76 Å for U-U respectively. As a measure of stoichiometry change, the lattice parameter between pre-heating and recovered (post

melting) samples was measured to be ~0.1%. This change is consistent with a stoichiometry change UO_{2+x} where x is less than ± 0.005 ²⁷⁻²⁹ between the initial UO_2 and final UO_{2+x} samples.

Acknowledgements.

Thanks to Rick Spence and Altug Hasozbek for technical support and useful discussions. This work was supported by the U.S. Department of Energy (DOE), office of Basic Energy Sciences (BES), BES DE-FG02-09ER46650 (MD simulations, analysis and manuscript preparation, L. B. S. and J. B. P.), DOE SBIR DE SC0007564 (x-ray experiment, JKRW, AT, OLGA). The Advanced Photon Source, Argonne National Laboratory is funded under U.S. DOE, BES contract number DE-AC02-06CH11357.

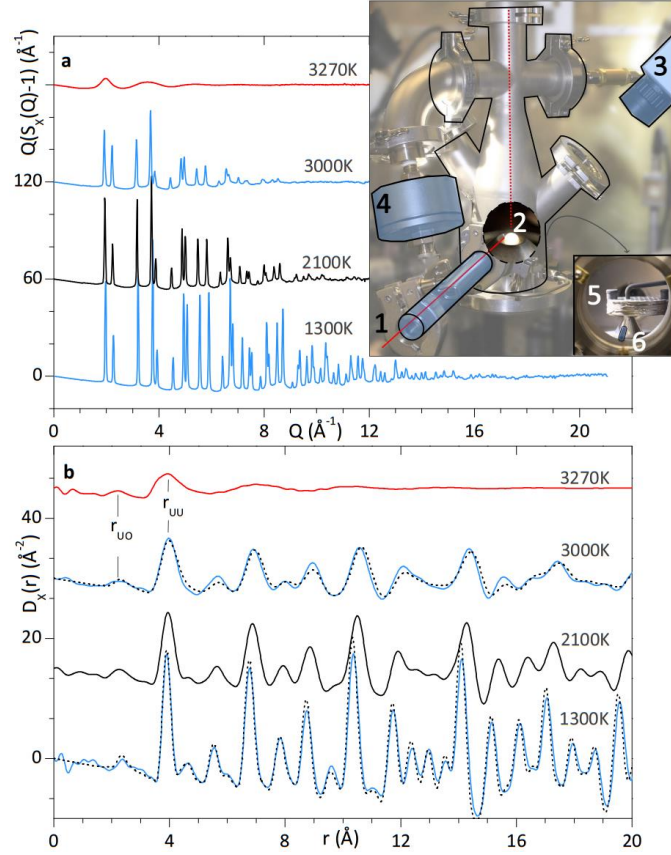


Fig. 1 **a** Measured x-ray structure factor patterns for UO_2 . The setup diagram (INSET) shows the incident x-ray beam passing through the lead-lined collimator (1), the hot molten sample in the chamber (2), and the pyrometer (3). The HEPA filter for exhaust gas (4), and the view through the backside window shows the sample loader (5) and Secondary Beam stop (6), which absorbed the exit window background scattering. **b** Measured x-ray pair distribution functions $D_x(r)$, generated from the patterns in A. The dotted lines are from the Yakub MD model, the 3270K lines are plotted in red to indicate the liquid state.

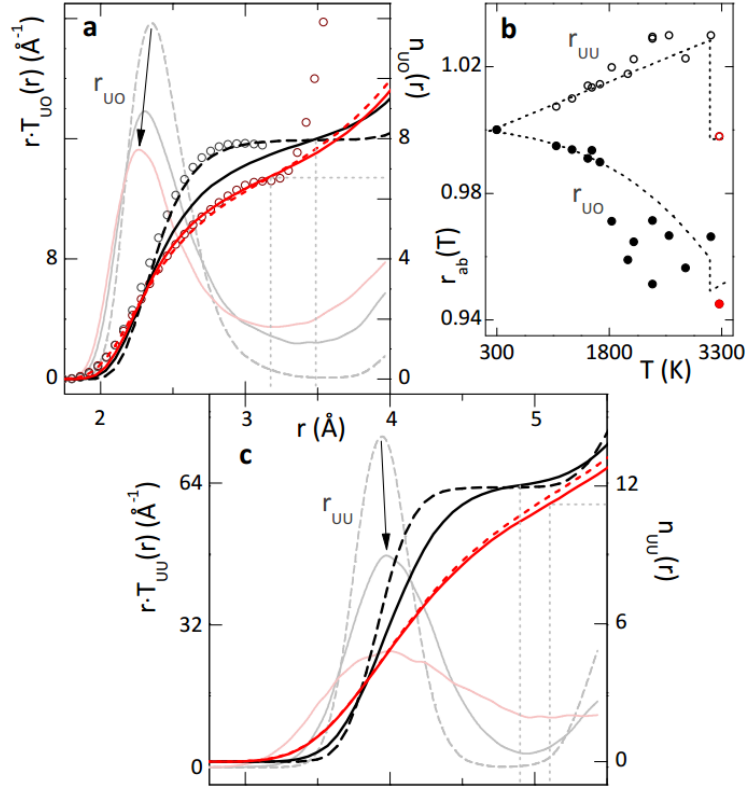


Fig. 2. **a** The open circles are the measured running coordination numbers $n_{uo}(r)$ from the x-ray measurements at 2100K and 3270K. Note that above 3 \AA U-U correlations also contribute significantly to these $n_{uo}(r)$ measurements. In **a**, **c** U-O (**a**) and U-U (**c**) pair distribution functions ($rT(r)$), and $n(r)$ patterns from the Yakub MD model are at three temperatures: In the solid state either side of the lambda transition at 2100K and 3000K (dashed black and unbroken black curves = $n(r)$), and the third in the liquid state at 3270K (red curves = $n(r)$). The light grey and light red curves are the corresponding $rT(r)$ patterns. The red short dashed curves are the 3270K $n(r)$ patterns from the refined MD model. **b** Measured r_{uo} (solid circles) and r_{uu} (open circles), divided by the 300K value. The dotted lines are the MD model. Red (or grey) circles indicate the liquid state measurement.

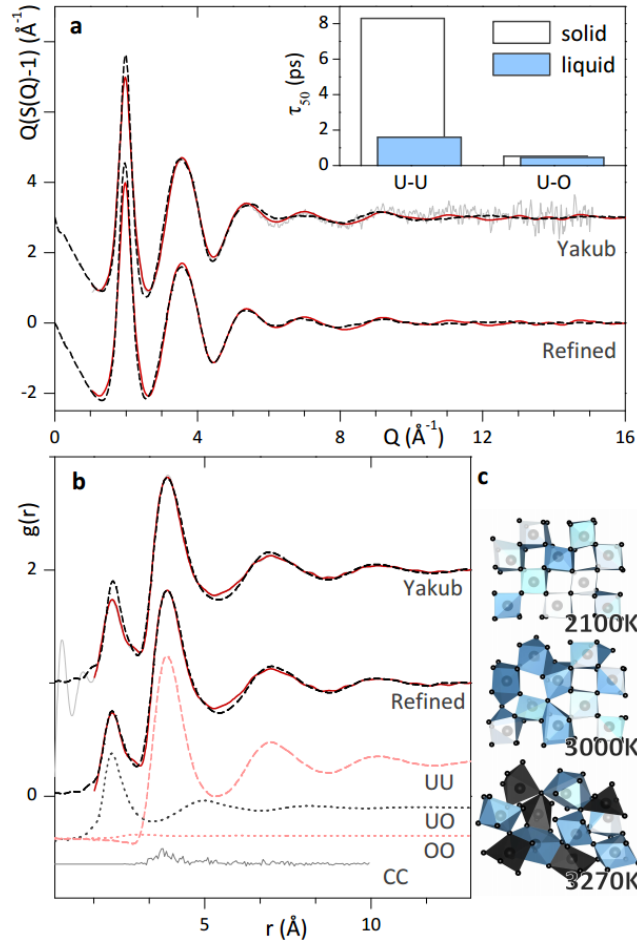


Fig. 3. Diffraction measurements (red or grey) vs. the Yakub and refined MD models (black dashed). **a** The thin, light grey line on the upper pattern is the raw measurement, whereas the smoother red (or grey) lines correspond to the same colored line in **b**. INSET are the times for 50% of UO or UU bonds to be broken in the solid or supercooled liquid both at 3000K (light red or grey). **b** The solid red (or grey) lines were filtered by Fourier transforming with an r -dependent modification function to reduce unphysical high frequency noise^{13,14}, whereas the solid light grey line show the unmodified transform. The lower dashed and dotted curves are the UU, UO and OO partial contributions to the total x-ray pattern. The lowermost curve is the concentration-concentration distribution function for U6 and U7 subspecies (mainly UO_6 and UO_7 , see main text). The small positive peak on the cc curve indicates slight clustering of U6-U6 and U7-U7 nearest neighbors. **c** Slices from the refined MD simulation ($\sim 15 \times 12 \times 3 \text{ \AA}$) showing U-O polyhedra, above and below the lambda transition (2100K, 3000K) and in the liquid state (3270K). The bottom slice shows the liquid again, redrawn as U6 (black) and U7 (light blue or grey) polyhedra.

References

1. Fink, J. K. Thermophysical properties of uranium dioxide. *J. Nucl. Mater.* **279**, 1–18 (2000).
2. Manara, D. *et al.* The Melting Behaviour of Oxide Nuclear Fuels: Effects of the Oxygen Potential Studied by Laser Heating. *Procedia Chem.* **7**, 505–512 (2012).
3. Manara, D., Ronchi, C., Sheindlin, M., Lewis, M. & Brykin, M. Melting of stoichiometric and hyperstoichiometric uranium dioxide. *J. Nucl. Mater.* **342**, 148–163 (2005).
4. Welland, M. J., Thompson, W. T., Lewis, B. J. & Manara, D. Computer simulations of non-congruent melting of hyperstoichiometric uranium dioxide. *J. Nucl. Mater.* **385**, 358–363 (2009).
5. Yakub, E., Ronchi, C. & Staicu, D. Molecular dynamics simulation of premelting and melting phase transitions in stoichiometric uranium dioxide. *J. Chem. Phys.* **127**, 094508 (2007).
6. Günay, S. D., Akdere, ü. & Taşseven, ç. Hypernetted chain calculations of molten uranium dioxide: Comparison of rigid ion potentials. *J. Mol. Liq.* **173**, 124–129 (2012).
7. Arima, T., Yamasaki, S., Inagaki, Y. & Idemitsu, K. Evaluation of thermal properties of UO₂ and PuO₂ by equilibrium molecular dynamics simulations from 300 to 2000K. *J. Alloys Compd.* **400**, 43–50 (2005).
8. Basak, C. B., Sengupta, A. K. & Kamath, H. S. Classical molecular dynamics simulation of UO₂ to predict thermophysical properties. *J. Alloys Compd.* **360**, 210–216 (2003).
9. Morelon, N.-D., Ghaleb, D., Delaye, J.-M. & Van Brutzel, L. A new empirical potential for simulating the formation of defects and their mobility in uranium dioxide. *Philos. Mag.* **83**, 1533–1555 (2003).
10. Winborne, D. A., Nordine, P. C., Rosner, D. E. & Marley, N. F. Aerodynamic levitation technique for containerless high temperature studies on liquid and solid samples. *Metall. Trans. B* **7**, 711–713 (1976).

11. Fischer, H. E., Barnes, A. C. & Salmon, P. S. Neutron and x-ray diffraction studies of liquids and glasses. *Rep. Prog. Phys.* **69**, 233–299 (2006).
12. Lewis, G. V. & Catlow, C. R. A. Potential models for ionic oxides. *J. Phys. C Solid State Phys.* **18**, 1149–1161 (1985).
13. Skinner, L. B. *et al.* Joint diffraction and modeling approach to the structure of liquid alumina. *Phys. Rev. B* **87**, (2013).
14. Skinner, L. B. *et al.* A time resolved high energy X-ray diffraction study of cooling liquid SiO₂. *Phys. Chem. Chem. Phys.* **15**, 8566 (2013).
15. Hennet, L. *et al.* Development of structural order during supercooling of a fragile oxide melt. *J. Chem. Phys.* **126**, 074906 (2007).
16. Lou, H. *et al.* Negative expansions of interatomic distances in metallic melts. *Proc. Natl. Acad. Sci.* **110**, 10068–10072 (2013).
17. Bhatia, A. B. & Thornton, D. E. Structural Aspects of the Electrical Resistivity of Binary Alloys. *Phys. Rev. B* **2**, 3004–3012 (1970).
18. Salikhov, T. P. & Kan, V. V. Radiative Properties of Uranium Dioxide Near Its Melting Point. *Int. J. Thermophys.* **20**, 163–1176 (1999).
19. Skinner, L. B., Benmore, C. J. & Parise, J. B. Area detector corrections for high quality synchrotron X-ray structure factor measurements. *Nucl. Instrum. Methods Phys. Res. Sect. Accel. Spectrometers Detect. Assoc. Equip.* **662**, 61–70 (2012).
20. Hammersley, A. P., Svensson, S. O., Hanfland, M., Fitch, A. N. & Hausermann, D. Two-dimensional detector software: From real detector to idealised image or two-theta scan. *High Press. Res.* **14**, 235–248 (1996).
21. Skinner, L. B. *et al.* Low Cation Coordination in Oxide Melts. *Phys. Rev. Lett.* **112**, (2014).
22. Su, Z. & Coppens, P. Relativistic X-ray Elastic Scattering Factors for Neutral Atoms $Z = 1-54$ from Multiconfiguration Dirac–Fock Wavefunctions in the $0-12\text{\AA}^{-1} \sin\theta/\lambda$ Range, and Six-Gaussian Analytical Expressions in the $0-6\text{\AA}^{-1}$ Range. *Acta Crystallogr. A* **53**, 749–762 (1997).

23. Rez, D., Rez, P. & Grant, I. Dirac–Fock calculations of X-ray scattering factors and contributions to the mean inner potential for electron scattering. *Acta Crystallogr. A* **50**, 481–497 (1994).
24. Waasmaier, D. & Kirfel, A. New analytical scattering-factor functions for free atoms and ions. *Acta Crystallogr. A* **51**, 416–431 (1995).
25. Smith, W. & Forester, T. R. DL_POLY_2.0: A general-purpose parallel molecular dynamics simulation package. *J. Mol. Graph.* **14**, 136–141 (1996).
26. Desgranges, L., Baldinozzi, G., Rousseau, G., Nièpce, J.-C. & Calvarin, G. Neutron Diffraction Study of the in Situ Oxidation of UO_2 . *Inorg. Chem.* **48**, 7585–7592 (2009).
27. Blackburn, P. E., Weissbart, J. & Gulbransen, E. A. Oxidation of Uranium Dioxide. *J. Phys. Chem.* **62**, 902–908 (1958).
28. Schmitz, F., Dean, G. & Halachmy, M. Application of lattice constant measurements for stoichiometry determination in irradiated U-Pu mixed oxide fuels. *J. Nucl. Mater.* **40**, 325–337 (1971).
29. Norris, D. I. R. & Kay, P. Oxygen potential and lattice parameter measurements in $(\text{U}, \text{Ce})\text{O}_2 - \text{zx}$. *J. Nucl. Mater.* **116**, 184–194 (1983).